Mechanism and Machine Theory 143 (2020) 103618

Contents lists available at ScienceDirect

Mechanism and Machine Theory

journal homepage: www.elsevier.com/locate/mechmachtheory

Research paper

On the modeling of a contact-aided cross-axis flexural pivot

Pietro Bilancia[a,*], Giovanni Berselli[a], Spencer Magleby[b], Larry Howell[b]

[a] Department of Mechanical, Energy, Management and Transportation Engineering, University of Genova, Genova 16145, Italy
[b] Department of Mechanical Engineering, Brigham Young University, Provo, 84602, Utah, United States

ARTICLE INFO

Article history:
Received 30 July 2019
Revised 5 September 2019
Accepted 12 September 2019

Keywords:
Cross-Axis Flexural Pivot
Contact-aided compliant mechanism
Chained-beam-constraint model
Multi software framework

ABSTRACT

This paper reports the study of a planar Cross-Axis Flexural Pivot (CAFP) comprising an additional contact pair. The proposed device may be useful for applications requiring a revolute joint that behaves differently when deflecting clockwise/anti-clockwise. The presence of the contact pair reduces the free length of one flexures, resulting in a considerable increment of the overall joint stiffness. The pivot behaviour is investigated, for different load cases, via the Chained-Beam-Constraint Model (CBCM), namely an accurate method to be applied in large deflection problems. A framework comprising Matlab and ANSYS is developed for testing the CAFP performances in terms of rotational stiffness, parasitic shift and maximum stress, with different combinations of geometrical aspect ratios and contact extensions. Results achieved via CBCM for a pure rotation applied to the CAFP's output link are then verified through Finite Element Analysis. The resulting performance maps show good agreement between the numerical results. Furthermore, the CBCM shows an improved computational efficiency, which is a crucial aspect for preliminary design steps. At last, direct comparison between simulations and experiments, developed by means of two custom test rigs, confirms the efficacy of the proposed design method for the modeling of contacts in large deflection problems.

1. Introduction

The Cross-Axis Flexural Pivot (CAFP) is a planar beam-based compliant mechanism (CM) [1], formed by two symmetric beams, that are connected at both ends to a pair of shared rigid blocks [2], hereafter referred to as ground and output links. Two different configurations have been conceived in literature: in the first one the crossing beams are completely independent, whereas in the second one, usually referred as cartwheel pivot, the beams are connected to each other where they cross, producing a single structure. As highlighted by Valentini and Pennestrì [3], the resulting elasto-kinematic behaviour shows remarkable differences based on the selected configuration. In particular, the first configuration is characterized by an increasing nonlinear trend of the equivalent stiffness for very large deflections, whereas the second configuration presents the typical trend of circular and elliptical flexural hinges, namely a reduction of the equivalent stiffness as the angle of rotation increases.

When employed in place of a revolute joint, the CAFP morphology enables a highly selective compliant behaviour [4,5], namely a low stiffness for in-plane motion and high stiffness along other directions. Due to potential advantages over common rigid kinematic pairs, such as the absence of backlash and friction, the high positioning accuracy, and the reduced

* Corresponding author.
E-mail address: pietro.bilancia@edu.unige.it (P. Bilancia).

https://doi.org/10.1016/j.mechmachtheory.2019.103618
0094-114X/

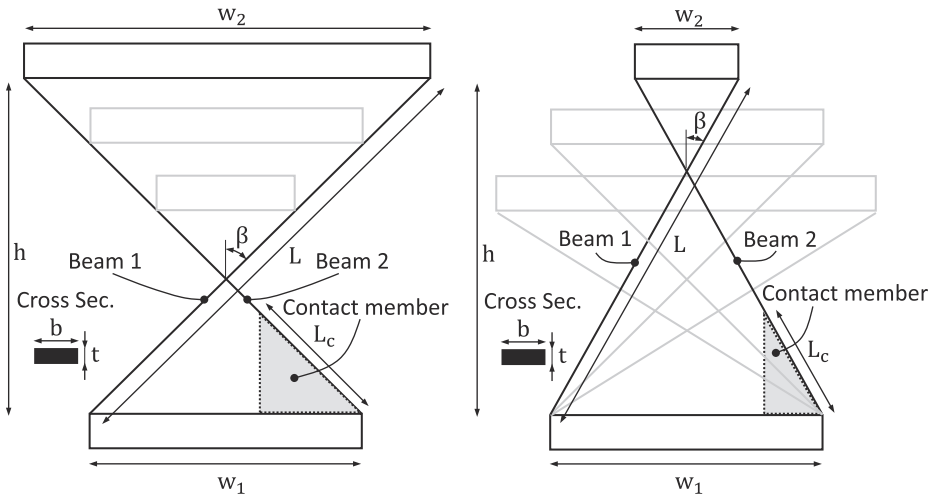

(a) Configurations with $\beta = \text{const.}$ (b) Configurations with $L = \text{const.}$

Fig. 1. Contact-aided parametric CAFP.

number of components (thus the simplified manufacturing process), the CAFP concept is commonly implemented in precision engineering applications [6]. Examples include measurement systems [7], precision mechanisms [8–11], optical instruments [12], bio-inspired devices [13] and space systems [14]. The relatively simple CAFP topology allows to easily form arrays [15] or to combine the mechanism with additional structural elements to synthesize static-balanced mechanisms [16–19]. As a result of the advent of efficient additive manufacturing technologies, even more complex shapes can be produced [11,18,20]. Furthermore, by combining typical origami principles and two-dimensional machining processes, folded CAFP joints can be manufactured [21].

However, as a CM, the CAFP analysis/design is more complex and some critical structural issues have to be considered. In the literature, several works are focused on the CAFP performance analysis. Apart from the fatigue life [22], which has to be carefully investigated in case of dynamic operative conditions, the CAFP's beams can fail due to buckling in case of compressive loads acting on the ground and output rigid links [2]. From a kinematic standpoint, the CAFP's maximum deflection is naturally limited by the stress field arising within the flexures [23] and it is usually constrained in the range $[0, \pi/2]$, depending on the employed material. This aspect restricts the use of the CAFP to applications that need a limited well-defined deflection range. Also, the relative rotation between the ground and output links entails a parasitic shift from the initial center of rotation, i.e. the intersection point between the flexures in the undeflected configuration [24–28]. CAFP analysis and design can be addressed via various approaches. For example, models employing the linear Euler-Bernoulli beam theory for small angles of deflections are reported in [2,6]. In [2], the large deflection problem is solved by means of elliptic integrals for a pure moment load case. This method provides an exact solution and it is suitable for relative simple case studies that involve slender beams with an uniform cross section. In [29], the CAFP is studied resorting to the Pseudo-Rigid Body (PRB) method, allowing the use of common theories related to rigid-body mechanisms. In [30], the dynamic spline formulation is used to simulate both static and dynamic CAFP behaviour. In [23,25], the CAFP under the effect of both forces and moment is modeled resorting to the Beam-Constraint Model (BCM) [31,32], i.e. a closed-form technique capable of capturing nonlinearities when deflections are within $(10 - 15)\%$ of the flexures length. This latter limit has been recently overcome by the introduction of the so-called Chained-Beam-Constraint Model (CBCM) [33–35], namely an innovative discretization-based approach to be applied for the modeling of beam-based CMs under different boundary conditions and load case scenarios. The CBCM divides a single flexure in more elements, each of them modeled by BCM equations. The closed-form formulation allows to solve the CAFP deflection via numerical approaches [33], resulting in a computational efficiency comparable to 1D Finite Element Analysis (FEA) [27].

Building on this solution, the present paper provides the modeling of a contact-aided [36,37] CAFP under various planar load conditions. The study aims at testing the CBCM efficiency in presence of contact formulation, both in terms of results accuracy and simulation time. This aspect becomes relevant for parametric studies, in which several simulations have to be performed to investigate the response of the system with different input parameters. The proposed device, whose principle schematic is represented in Fig. 1, is composed of two disconnected independent beams located in parallel planes. A purposely shaped contact member [38], fixed to the ground link, is introduced to reduce the free length of one flexure and thus to increment the total CAFP stiffness whenever a deflection is enforced. Overall, the CAFP behaves differently when deflecting either clockwise or anti-clockwise. A possible application of this concept may be found in bio-inspired robotic wrist mechanisms [39]. In fact, as specified in [40], the human wrist exhibits a major passive stiffness (i.e. the stiffness due to the presence of the muscles in the forearm) during the radial deviation than that of the ulnar deviation. The aforementioned

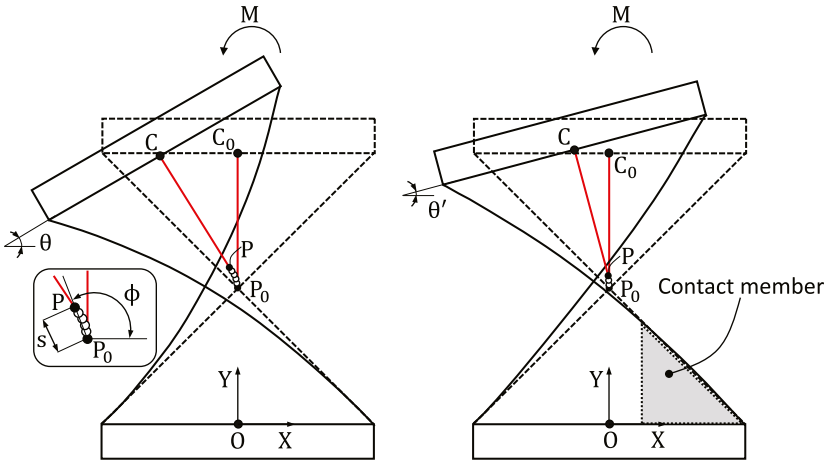

(a) Standard CAFP - deflected configuration. (b) Contact-aided CAFP - deflected configuration.

Fig. 2. Effect of the contact member on the pivot deflection.

asymmetry can be obtained by implementing the proposed contact-aided CAFP as a compliant transmission element in the wrist.

As a result of the parametric studies, in this paper different performance maps for joint stiffness, parasitic shift and maximum stress are reported to enable designers to visualize the advantages/limits of the joint during the preliminary design steps. Numerical data, obtained via a custom software framework [41,42] allowing the use of CBCM and batch 1D FEA, are finally validated by experimental investigations for different planar loads. Two experimental setups are used to measure both the rotational stiffness and the parasitic shift. The rest of the paper is organized as follows: Section 2 provides information about the mechanical system considered in the current study, Section 3 reports the CBCM mathematical formulation, Section 4 describes the software framework architecture and its main features, Section 5 reports the numerical results achieved on the pivot enforcing a pure rotation, Section 6 reports a comparison between numerical and experimental results for two different load conditions, whereas Section 7 summarizes the concluding remarks.

2. Contact-aided pivot

This section provides a description of the mechanical model, focusing on design variables and performance criteria to be used for the subsequent analysis. With reference to Fig. 1, taking into consideration a symmetric CAFP composed of two independent flexures with constant rectangular cross section, the pivot geometry is completely defined by h, L, w_1, w_2, b and t, namely the pivot height, the flexure length, the lower and upper width, and the cross section dimensions. The semi-angle between flexures is given by the following trigonometric formula:

$$\beta = \arcsin((w_1 + w_2)/2L) \tag{1}$$

According to Fig. 1(a) and (b) and Eq. 1, given w_1, the aspect ratio, defined as $AR = w_2/w_1$, can be varied by assuming a constant angle (i.e. $\beta = \text{const}$) or a constant flexure length (i.e. $L = \text{const}$). As evident from Fig. 1(b), the second option is characterized by a minor variation range. In this work a purposely shaped contact member, shown in Figs. 1 and 2, is introduced at the base of the pivot, allowing an increment in the joint stiffness. As visible in Fig. 2(a) and (b), a pure moment M applied on the upper rigid body provides a deflection $\theta' < \theta$ whenever the contact is considered, due to an evident reduction, in the order of L_c, of the flexure *(Beam 2)* free length. Also the parasitic shift, identified by module $s = \overline{PP_0}$ and phase ϕ, as in Fig. 2, is influenced by the presence of the contact. In the following sections, the behaviour of the contact-aided pivot, in terms of rotational stiffness, parasitic shift and maximum stress is investigated for different combinations of AR (by considering $\beta = \text{const}$ or $L = \text{const}$) and L_c. The pivot is initially loaded by applying a pure rotation to the output link. Then, single effects of a horizontal force acting on the output link or of a rotation applied to a constrained point placed in the initial intersection between the flexures (i.e. P_0 in Fig. 2), are studied with both numerical (CBCM and FEA) and experimental approaches.

3. CBCM formulation

3.1. Static modeling under planar loads

Following the work reported in [33], a CAFP's flexure can be discretized into N elements of equal length $L_{el} = L/N$, each of them locally described by BCM equations [31,32]. Assuming a constant rectangular cross section, defined by b and t, the

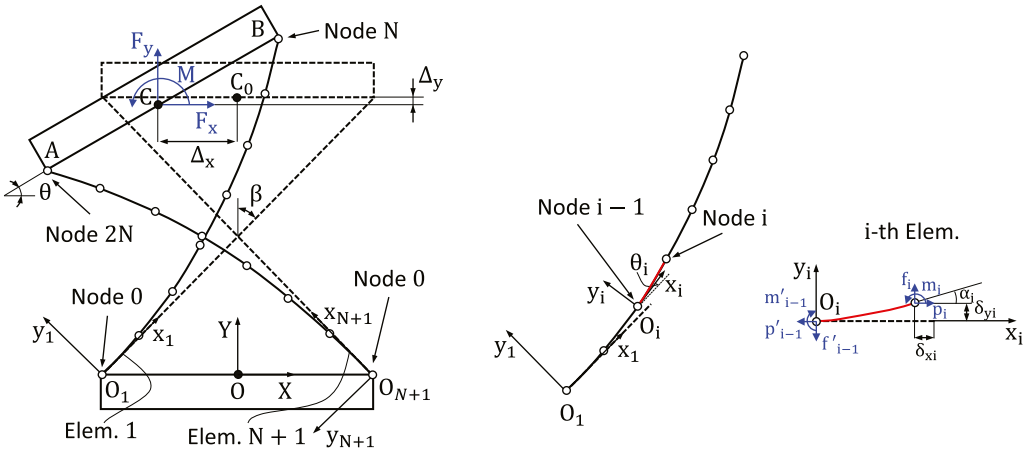

(a) CAFP schematic: global loads and displacements.

(b) Analysis of the *i*-th element.

Fig. 3. CBCM model.

load-deflection characteristic of the *i*th element, shown in Fig. 3, is given by the following relations:

$$\begin{bmatrix} f_i \\ m_i \end{bmatrix} = \begin{bmatrix} 12 & -6 \\ -6 & 4 \end{bmatrix} \begin{bmatrix} \delta_{yi} \\ \alpha_i \end{bmatrix} + p_i \begin{bmatrix} 6/5 & -1/10 \\ -1/10 & 2/15 \end{bmatrix} \begin{bmatrix} \delta_{yi} \\ \alpha_i \end{bmatrix} + p_i^2 \begin{bmatrix} -1/700 & 1/1400 \\ 1/1400 & -11/6300 \end{bmatrix} \begin{bmatrix} \delta_{yi} \\ \alpha_i \end{bmatrix} \tag{2}$$

$$\delta_{xi} = \frac{t^2 p_i}{12 L_{el}} - 0.5 \begin{bmatrix} \delta_{yi} & \alpha_i \end{bmatrix} \begin{bmatrix} 6/5 & -1/10 \\ -1/10 & 2/15 \end{bmatrix} \begin{bmatrix} \delta_{yi} \\ \alpha_i \end{bmatrix} - p_i \begin{bmatrix} \delta_{yi} & \alpha_i \end{bmatrix} \begin{bmatrix} -1/700 & 1/1400 \\ 1/1400 & -11/6300 \end{bmatrix} \begin{bmatrix} \delta_{yi} \\ \alpha_i \end{bmatrix} \tag{3}$$

where δ_{xi}, δ_{yi} and α_i are the displacements and rotation of the *i*th element at node *i* (referred to the local *i*th coordinate system, placed in the node *i*-1 as shown in Fig. 3(b)) normalized with respect to L_{el}, and p_i, f_i and m_i are the forces and moment normalized with respect to EI/L_{el}^2 and EI/L_{el}, where E is the material elastic modulus and $I = bt^3/12$ is the cross section moment of inertia. The first terms of Eqs. (2) and (3) define the linear approximation, which is valid for describing the behaviour of a cantilever beam under tip loads in case of small deflections. The CAFP's behaviour is well captured in the middle range of deflections by applying the BCM equations on the flexures, i.e. by using a unique element $L_{el} = L$ for each of the beams, as proved in [23,25]. The modeling of two series of N elements for the whole CAFP's structure leads to a remarkable increment in the number of variables.

With reference to Fig. 3(a), being known any combination of three parameters among the global external loads (i.e. F_x, F_y and M) and the global displacements (i.e. Δ_x, Δ_y and θ), the total number of variables to be determined for solving the CBCM problem is 12*N*+7, namely:

- δ_{xi}, δ_{yi}, α_i, p_i, f_i, m_i, for $i = 1, \ldots, 2N$ (12*N* entities);
- the remaining set containing the undefined global loads and/or displacements (3 entities);
- the coordinate of point A (x_A, y_A) and point B (x_B, y_B) with respect to the coordinate systems $O_{N+1}x_{N+1}y_{N+1}$ and $O_1x_1y_1$ respectively (4 entities).

Therefore, to ensure a closed-form solution for the problem, 12*N*+7 relations between the aforementioned variables have to be defined. Besides the 6*N* BCM load-deflection characteristics (3 for each of the 2*N* CAFP elements), expressed by Eqs. (2) and (3), the remaining relations refer to the local and global equilibrium and to the geometrical constraints.

By analyzing the free-body diagram proposed in Fig. 3(b), the following local static equilibrium equations for the *i*th element hold:

$$\begin{bmatrix} f'_{i-1} \\ p'_{i-1} \\ m'_{i-1} \end{bmatrix} = \begin{bmatrix} 1 & 0 & 0 \\ 0 & 1 & 0 \\ (1+\delta_{xi}) & -\delta_{yi} & 1 \end{bmatrix} \begin{bmatrix} f_i \\ p_i \\ m_i \end{bmatrix} \tag{4}$$

where p'_{i-1}, f'_{i-1}, m'_{i-1} are the loads applied by the (*i*-1)th element to the *i*th element at node *i*-1, mathematically obtained by applying a vectorial rotation of α_{i-1} (i.e. the angle between $O_ix_iy_i$ and $O_{i-1}x_{i-1}y_{i-1}$) to the tip loads p_{i-1}, f_{i-1} and m_{i-1}:

$$\begin{bmatrix} f_{i-1} \\ p_{i-1} \\ m_{i-1} \end{bmatrix} = \begin{bmatrix} \cos\alpha_{i-1} & -\sin\alpha_{i-1} & 0 \\ \sin\alpha_{i-1} & \cos\alpha_{i-1} & 0 \\ 0 & 0 & 1 \end{bmatrix} \begin{bmatrix} f'_{i-1} \\ p'_{i-1} \\ m'_{i-1} \end{bmatrix} \tag{5}$$

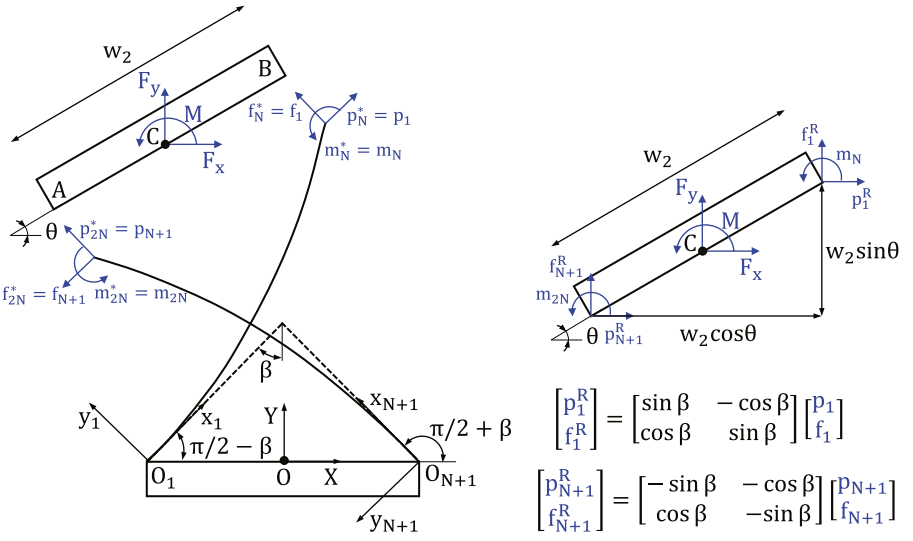

(a) Free-body diagram of the overall CAFP. (b) Detailed view.

Fig. 4. CAFP global equilibrium.

By considering the angle $\theta_i = \sum_1^{i-1} \alpha_i$ between $O_i x_i y_i$ and $O_1 x_1 y_1$, the equilibrium equation of the ith element can be re-written as follows:

$$\begin{bmatrix} f_1 \\ p_1 \\ m_{i-1} \end{bmatrix} = \begin{bmatrix} \cos\theta_i & -\sin\theta_i & 0 \\ \sin\theta_i & \cos\theta_i & 0 \\ (1+\delta_{xi}) & -\delta_{yi} & 1 \end{bmatrix} \begin{bmatrix} f_i \\ p_i \\ m_i \end{bmatrix} \quad i = 2, \ldots, N \tag{6}$$

and, for the second CAFP's flexure, which refers to $O_{N+1} x_{N+1} y_{N+1}$ as visible in Fig. 3(a), the following relation holds:

$$\begin{bmatrix} f_{N+1} \\ p_{N+1} \\ m_{i-1} \end{bmatrix} = \begin{bmatrix} \cos\theta_i & -\sin\theta_i & 0 \\ \sin\theta_i & \cos\theta_i & 0 \\ (1+\delta_{xi}) & -\delta_{yi} & 1 \end{bmatrix} \begin{bmatrix} f_i \\ p_i \\ m_i \end{bmatrix} \quad i = N+2, ., 2N \tag{7}$$

Equations (6) and (7) form 6(N-1) relations of the CBCM system. The global equilibrium can be defined by taking into account the external loads F_x, F_y and M applied at point C, as well as the tip loads of the elements N and $2N$, which can be expressed in the coordinate system $O_1 x_1 y_1$ and $O_{N+1} x_{N+1} y_{N+1}$ respectively, being:

$$\begin{bmatrix} f_N^* \\ p_N^* \\ m_N^* \end{bmatrix} = \begin{bmatrix} f_1 \\ p_1 \\ m_N \end{bmatrix} = \begin{bmatrix} \cos\theta_N & -\sin\theta_N & 0 \\ \sin\theta_N & \cos\theta_N & 0 \\ 0 & 0 & 1 \end{bmatrix} \begin{bmatrix} f_N \\ p_N \\ m_N \end{bmatrix} \quad \begin{bmatrix} f_{2N}^* \\ p_{2N}^* \\ m_{2N}^* \end{bmatrix} = \begin{bmatrix} f_{N+1} \\ p_{N+1} \\ m_{2N} \end{bmatrix} = \begin{bmatrix} \cos\theta_{2N} & -\sin\theta_{2N} & 0 \\ \sin\theta_{2N} & \cos\theta_{2N} & 0 \\ 0 & 0 & 1 \end{bmatrix} \begin{bmatrix} f_{2N} \\ p_{2N} \\ m_{2N} \end{bmatrix} \tag{8}$$

Therefore, with reference to Fig. 4, by rotating $O_1 x_1 y_1$ and $O_{N+1} x_{N+1} y_{N+1}$ of $-(\pi/2 - \beta)$ and $-(\pi/2 + \beta)$ respectively, the following 3 equilibrium relations can be added to the system:

$$\begin{bmatrix} F_x \\ F_y \end{bmatrix} = \frac{EI}{L_{el}^2} \begin{bmatrix} \sin\beta & -\cos\beta \\ \cos\beta & \sin\beta \end{bmatrix} \begin{bmatrix} p_1 \\ f_1 \end{bmatrix} + \frac{EI}{L_{el}^2} \begin{bmatrix} -\sin\beta & -\cos\beta \\ \cos\beta & -\sin\beta \end{bmatrix} \begin{bmatrix} p_{N+1} \\ f_{N+1} \end{bmatrix} \tag{9}$$

$$M = \frac{EI}{L_{el}} m_N + \frac{EI}{L_{el}} m_{2N} + w_2 \frac{EI}{L_{el}^2} \begin{bmatrix} \sin\theta & -\cos\theta \end{bmatrix} \begin{bmatrix} -\sin\beta & -\cos\beta \\ \cos\beta & -\sin\beta \end{bmatrix} \begin{bmatrix} p_{N+1} \\ f_{N+1} \end{bmatrix} + 0.5 w_2 \begin{bmatrix} \sin\theta & -\cos\theta \end{bmatrix} \begin{bmatrix} -F_x & -F_y \end{bmatrix} \tag{10}$$

For both the pivot's flexures, the overall displacements and rotation at the extremities A and B (see Fig 3(a)) are related to the local entities δ_{xi}, δ_{yi} and α_i. Consequently, 6 constraint geometric equations must be enforced in the model. For the first flexure, which refers to $O_1 x_1 y_1$, it is possible to write:

$$\begin{bmatrix} x_B \\ y_B \end{bmatrix} = \sum_{i=1}^{N} \left[\begin{bmatrix} \cos\theta_i & -\sin\theta_i \\ \sin\theta_i & \cos\theta_i \end{bmatrix} \begin{bmatrix} L_{el}(1+\delta_{xi}) \\ L_{el}\delta_{yi} \end{bmatrix} \right] \qquad \theta_N + \alpha_N = \theta \tag{11}$$

and, for the second beam, by considering $O_{N+1} x_{N+1} y_{N+1}$, becomes:

$$\begin{bmatrix} x_A \\ y_A \end{bmatrix} = \sum_{i=N+1}^{2N} \left[\begin{bmatrix} \cos\theta_i & -\sin\theta_i \\ \sin\theta_i & \cos\theta_i \end{bmatrix} \begin{bmatrix} L_{el}(1+\delta_{xi}) \\ L_{el}\delta_{yi} \end{bmatrix} \right] \qquad \theta_{2N} + \alpha_{2N} = \theta \tag{12}$$

Note that, for i=1 and $i = N$+1, the local reference coincides with the fixed coordinate systems, $O_1x_1y_1$ and $O_{N+1}x_{N+1}y_{N+1}$, and thus $\theta_1 = 0$ and $\theta_{N+1} = 0$. The global displacements of the output link during the pivot deflection, Δ_x and Δ_y, can be expressed with respect to *OXY* by the following 2 equations:

$$\begin{bmatrix}\Delta_X\\ \Delta_Y\end{bmatrix} = 0.5\begin{bmatrix}-\sin\beta & -\cos\beta\\ \cos\beta & -\sin\beta\end{bmatrix}\begin{bmatrix}x_A\\ y_A\end{bmatrix} + 0.5\begin{bmatrix}\sin\beta & -\cos\beta\\ \cos\beta & \sin\beta\end{bmatrix}\begin{bmatrix}x_B\\ y_B\end{bmatrix} \tag{13}$$

The last 2 equations of the model provide the geometric loop closure, written as:

$$\begin{bmatrix}w_1 + w_2\cos\theta\\ w_2\sin\theta\end{bmatrix} = -\begin{bmatrix}-\sin\beta & -\cos\beta\\ \cos\beta & -\sin\beta\end{bmatrix}\begin{bmatrix}x_A\\ y_A\end{bmatrix} + \begin{bmatrix}\sin\beta & -\cos\beta\\ \cos\beta & \sin\beta\end{bmatrix}\begin{bmatrix}x_B\\ y_B\end{bmatrix} \tag{14}$$

The overall nonlinear system of 12N+7 equations can be numerically solved in Matlab environment resorting to a *fsolve* routine. The algorithm provides, as a result of the single analysis, a matrix containing the values of the 12N+7 variables for a series of r incremental substeps.

3.2. Contact force

Focusing on Figs. 1 and 2, the interaction between the *Beam 2* and the contact triangular member can be modeled at nodal level by two approaches. The first approach introduces the effect by adding, on the basis of L_c, some additional constraints (i.e. $\delta_{yi} = 0$) to the nodes in the range $[N+1, N+\text{round}\,(N(L_c/L))]$, where "round" defines an operator that returns the integer number of the argument. However, two main issues arise:

1. the bonded condition on those nodes does not allow to capture the real behaviour of the beam during the anti-clockwise deflection. In fact, in the contact area, the beam should manifest a limited, but not negligible, curvature. Similar results can be achieved by modeling a CAFP composed of flexures with different length, i.e. $L_1 = L$ and $L_2 = L - Lc$;
2. the convergence is reached after a large number of numerical iterations and thus the CBCM computational efficiency is considerably decreased.

The second approach operates on nodal forces instead of nodal displacements. Taking as a reference the *Augmented Lagrangian* algorithm from the ANSYS contact library, the contact normal and tangential forces, to be expressed in the CBCM nodes, can be written as follows:

$$f_{cn,i} = -k\delta_{yi}, \quad i = N+1, \ldots, N+\text{round}\,(N(L_c/L)) \tag{15}$$

$$f_{ct,i} = \mu f_{cn,i}, \quad i = N+1, \ldots, N+\text{round}\,(N(L_c/L)) \tag{16}$$

where k is the contact stiffness and μ is the static friction coefficient. Note that Eq. (15) represents a simplified version of the penalty class algorithms [43], in which dynamic effects (e.g. damping) are usually considered. The proposed contact presents a friction force that is almost null during the CAFP deflection, and thus only Eq. (15) is considered in this paper. From a practical standpoint, for $i = N+1, \ldots, N+\text{round}\,(N(L_c/L))$, Eq. (2) becomes:

$$\begin{bmatrix}f_i\\ m_i\end{bmatrix} = \begin{bmatrix}12 & -6\\ -6 & 4\end{bmatrix}\begin{bmatrix}\delta_{yi}\\ \alpha_i\end{bmatrix} + p_i\begin{bmatrix}6/5 & -1/10\\ -1/10 & 2/15\end{bmatrix}\begin{bmatrix}\delta_{yi}\\ \alpha_i\end{bmatrix} + p_i^2\begin{bmatrix}-1/700 & 1/1400\\ 1/1400 & -11/6300\end{bmatrix}\begin{bmatrix}\delta_{yi}\\ \alpha_i\end{bmatrix} + \begin{bmatrix}f_{cn,i}\\ 0\end{bmatrix} \tag{17}$$

In the reported CBCM model, the element length, L_{el}, is constant along the beams and thus round$(N(L_c/L))$ is used to ensure the stability of the problem, i.e. to select a precise nodes interval to be considered for the contact. To achieve a major sensibility in the contact analysis, i.e. to study slight variations of L_c, a fine mesh can be defined in the model by choosing a high value for N or by adopting the unequal discretization method [35]. However, both these solutions increase the computational cost, since:

- for the single candidate, the total number of equations to be solved is $12N + 7$ for each of the r substeps;
- a variable element length $L_{el}(i), i = 1, \ldots, 2N$ would complicate the software structure because several additional subroutines (e.g. *for* loops and *if-else* statements) must be added.

After a series of preliminary tests, in this work, $N = 10$ is used to ensure good accuracy and high computational efficiency (note that in [33], large deflections without contact analysis are solved with $N = 4$).

3.3. Performance indexes estimation

As previously introduced in Section 2, three different outputs are considered in this paper for the study of the contact-aided CAFP, namely the pivot stiffness, parasitic shift and maximum stress in deflected state. These performance indexes are derived from the aforementioned results matrix. Considering a quasi-linear torque deflection law for medium/large deflections (i.e. $\theta < 0.883$ rad), the stiffness, to be calculated in case of $F_x = F_y = 0$, can be directly obtained as the mean value of $K = \partial M(\theta)/\partial\theta$.

Then, by considering a rigid segment $\overline{CP} = \overline{C_0P_0} = (w_2/2)/\tan\beta$ as in Fig. 2, the position of point P with respect to a coordinate system placed in P_0 and oriented as OXY, is given by:

$$x_P = \Delta_x + ((w_2/2)/\tan\beta)\sin\theta \qquad y_P = \Delta_y - ((w_2/2)/\tan\beta)\cos\theta - (w_1/2)/(\tan\beta) \tag{18}$$

and thus the parasitic shift module and phase can be calculated as:

$$s = \sqrt{x_P^2 + y_P^2} \qquad \begin{cases} \phi = \arctan\left(\frac{y_P}{x_P}\right), & x_P > 0 \\ \phi = \pi/2, & x_P = 0 \\ \phi = \arctan\left(\frac{y_P}{x_P}\right) + \pi, & x_P < 0 \end{cases} \tag{19}$$

Lastly, the stress acting on the ith element can be viewed as a superposition of two components:

$$\sigma_i(x_i) = \sigma_{b,i}(x_i) + \sigma_{ax,i} \tag{20}$$

where $\sigma_{b,i}(x_i)$ is the bending stress along the x-coordinate of $O_i x_i y_i$, whereas $\sigma_{ax,i}$ is the tensile stress related to the stretch of the ith element under the axial force p_i, such that:

$$\sigma_{b,i}(x_i) = \frac{M(x_i)t/2}{I} \qquad \sigma_{ax,i} = \frac{p_i EI/L_{el}^2}{bt} \tag{21}$$

While $\sigma_{ax,i}$ is uniform along the ith element, $\sigma_{b,i}(x_i)$ requires the knowledge of $M(x_i)$, namely the dimensional moment acting along the ith element:

$$M(x_i) = \frac{EI}{\rho(x_i)} \tag{22}$$

The curvature is estimated for $x_i \in [0, 1]$ resorting to the following equation [33]:

$$\begin{cases} \frac{1}{\rho(x_i)} = \frac{1}{L_{el}}\left(\frac{\tanh(\sqrt{p_i})\cosh(x_i\sqrt{p_i}) - \sinh(x_i\sqrt{p_i})}{\sqrt{p_i}} f_i + \frac{\cosh(x_i\sqrt{p_i})}{\cosh(\sqrt{p_i})} m_i\right), & p_i \geq 0 \\ \frac{1}{\rho(x_i)} = \frac{1}{L_{el}}\left(\frac{\tan(\sqrt{-p_i})\cos(x_i\sqrt{-p_i}) - \sin(x_i\sqrt{-p_i})}{\sqrt{-p_i}} f_i + \frac{\cos(x_i\sqrt{-p_i})}{\cos(\sqrt{-p_i})} m_i\right), & p_i < 0 \end{cases} \tag{23}$$

At each analysis substep, the maximum stress σ_{Max} acting on the CAFP is then found as follows:

$$\sigma_{Max} = \max(\sigma_i,\ i = 0., 2N) \tag{24}$$

4. Software framework

The behaviour of the parametric contact-aided CAFP was investigated resorting to an integrated software framework [41,42], which exploits Matlab as a multi-tasks programming environment and ANSYS APDL as a nonlinear FEA solver capable of performing batch analysis. The mechanical models are solved employing CBCM method, following the procedure reported in Section 3, and then verified by means of the FEA approach. In particular, 1D FEA (beam elements) is used to test the CBCM performance both in terms of results accuracy and simulation time. A full factorial selection criteria [44] is used to perform a bi-dimensional Design of Experiments (DOEs) on the contact-aided CAFP, allowing the generation of the performance maps.

Based on the schematic depicted in Fig. 5, the framework is guided by a Matlab file, which is organized in four sections as follows:

1. In the first section, the user defines the *Input Parameters*, which comprise geometrical dimensions (L or β, w_1, b and t), material properties (E and ν), external loads (F_x, F_y and M) or displacements (Δ_x, Δ_y and θ), number of elements (N), number of substeps (r) and DOE spacing (number of points to be tested for each variables, i.e. AR and L_c);
2. In the second section, a *for* loop allows to perform the *DOE CBCM* by singularly testing each of the candidates, i.e. the $AR - L_c$ combinations, thanks to an external Matlab function (CAFP_CBCM.m), which implements all the equations discussed in Sections. 3.1 and 3.2. Once the numerical results of the single simulation are available, two additional functions (CAFP_Shift.m and CAFP_Stress.m) are launched for the evaluation of the performance indexes described in Section 3.3. The stiffness evaluation is performed in the main script by means of a simple numerical derivative followed by a mean value calculation.
3. In the third section, a *for* loop is used for the *DOE FEA*. In particular, by leveraging the ANSYS interfacing capabilities, a multi-software routine that can automatically solve all the candidates is implemented. For each analysis, Matlab exports the parameters vector (composed of the entities defined at point 1) into an external file (FEA_Input.txt) and provides the ANSYS batch launching. The parametric FE model, updated on the basis of the information stored in the previous file, exports the results of the nonlinear (NLGEOM option) analysis into FEA_Output.txt, which is then processed by Matlab.
4. In the last section, a *Results Comparison* is provided.

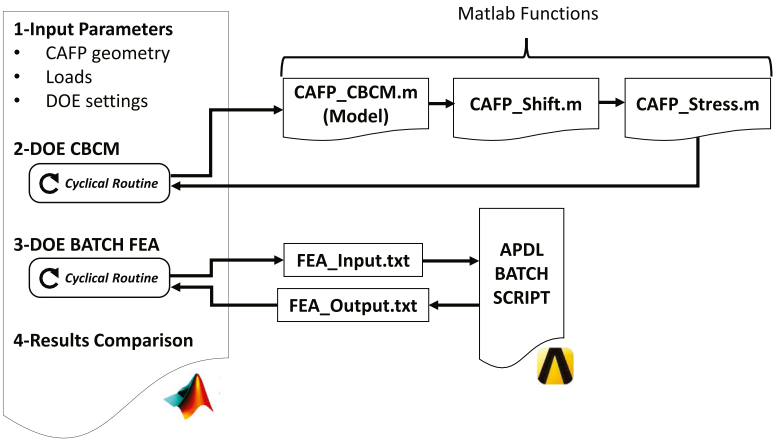

Fig. 5. Schematic of the framework used for the parametric studies.

Table 1
CAFP parameters adopted for testing the framework.

Parameter	Unit	Value(s)
N	–	10
t	mm	1.6
b	mm	5
w_1	mm	30
r	–	10
	β = const	
β	rad	$\pi/4$
AR	–	[0.5,3]
L_c	%L	[0,30]
	L = const	
L	mm	50
AR	–	[0.8,1.3]
L_c	%L	[0,30]

The FE model, whose geometry is automatically re-defined for each candidate, is composed of two identical beams connected by a rigid segment, characterized by a larger cross section. The lowest node set, composed of nodes 0 in Fig. 3(a), is fixed to the ground. A second rigid segment is placed in proximity of the *Beam 2* so as to model the contact. To ensure consistency with the CBCM models, the number of elements N is automatically imported in ANSYS. Each of the flexible beams is discretized with N *Beam 188* elements with quadratic shape functions, whereas *Conta 176* and *Targe 170* elements are used for the contact interaction. Furthermore, the *Augmented Lagrangian* contact formulation is enforced (*Key-option(2)=0*) in all the simulations. Then, in line with the CBCM, the external loads are applied in a series of r incremental substeps. The performance indexes are computed resorting to the relations presented in Section 3.3, except for the maximum Von Mises stress, which is directly provided by ANSYS. The proposed simulation code can be downloaded from the online reference to this work.

5. Numerical characterization of the pivot

This section reports the DOE results achieved on the pivot via the proposed numerical framework. Recalling Section 2, several combinations (AR, L_c) are tested for both the configurations reported in Fig. 1(a) and (b). All the candidates are guided in a pure rotation $\theta = 40^\circ = 0.7$ rad. Other load scenarios will be discussed in Section 6. The adopted material for the current application is Glycol-Modified Polyethylene Terephthalate (PETG), and the mechanical properties refer to a 3D printed (fused deposition modeling) bending specimen, obtained with a Prusa i3 Mk2 with 100% infill. The Young's modulus and Poisson's ratio are, respectively, $E = 1400$ MPa and $\nu = 0.4$, whereas the flexural yield strength is assumed equal to $\sigma_s = 45$ MPa. Parameter set and allowed range of variation for each geometrical parameter are summarized in Table 1. Figures 6 and 7 provide a comparison between the results obtained via CBCM and 1D FEA for the β = const and L = const configurations respectively. The data show a good agreement for each of the performance indexes, confirming the suitability of the CBCM for the analysis of large deflections and contact pairs. Moreover, as it may be seen in Fig. 7(a), the stiffness shows a remarkable variation in the design domain. This output highlights the possibility to exploit the L = const configuration (see Fig. 1(b)) for designing a rotational variable stiffness joint.

As discussed in Section 3.2, restricted ranges of L_c can be investigated by changing the value of N or by adopting the unequal discretization method [35]. The major source of discrepancy between the numerical results, obtained when $L_c = 30\%L$, may be attributed to the adopted contact algorithm. In the penalty algorithms, the amount of penetration between bodies depends on the normal stiffness k. Higher values of k reduce the penetration but can lead to convergence problems. To overcome this issue, ANSYS refines the value of k during the simulations [45]. On the contrary, in the current framework, the CBCM is solved with a constant value for k, causing differences in terms of penetration, that influence the processed results. To avoid this problem, k may be forced to be constant in ANSYS by means of a specific *Real Constant*, even though the problem convergence would be compromised, especially since r (i.e. the number of substeps) is kept constant. Alternatively, an iterative process that aims at refining the value of k can be implemented in the CBCM algoritmh. In both cases, the computational efficiency of the proposed framework would be considerably decreased. The simulations have been performed on a Workstation with an Intel(R) Core(TM) CPU @ 2.5 GHz and 16 GB RAM. Each CBCM model is solved in Matlab in 1.8 s, and a single APDL batch simulation takes 5.7 s to be completed. This aspect becomes relevant in the initial design steps, where several simulations have to be performed, such as for DOE or simulation purpose.

6. Experimental assessments

PETG physical prototypes of the $\beta = \text{const}$ configuration have been manufactured via 3D printing and tested resorting to two experimental setups. The tests aim at validating the accuracy of the proposed simulation framework for two different load scenarios: *(i)* a rotation θ applied to a constrained point P_0 of the workspace that forces the CAFP to follow a circular deflection path; *(ii)* a horizontal force F_x applied to the output link at point C.

6.1. Rotational setup

As visible from the results reported in Figs. 6(c) and (d) and 7(c) and (d) and in [29], the CAFP is subjected to an evident parasitic shift when a pure torque (or rotation) is applied to the outer link. The error between the resulting deflection path and an ideal circular path increases with the rotation. From a practical standpoint, this issue limits the use of a pure torque (or rotation) to the simulations. On the basis of these considerations and similarly to the previous literature [11,18,20], in this work, the experiments were conducted via a standard moment-deflection test rig. The system, shown in Fig. 8(a), is equipped with a worm-wheel gearset that acts on a main shaft, an Omega TQ103 socket calibrated torque sensor, and a US

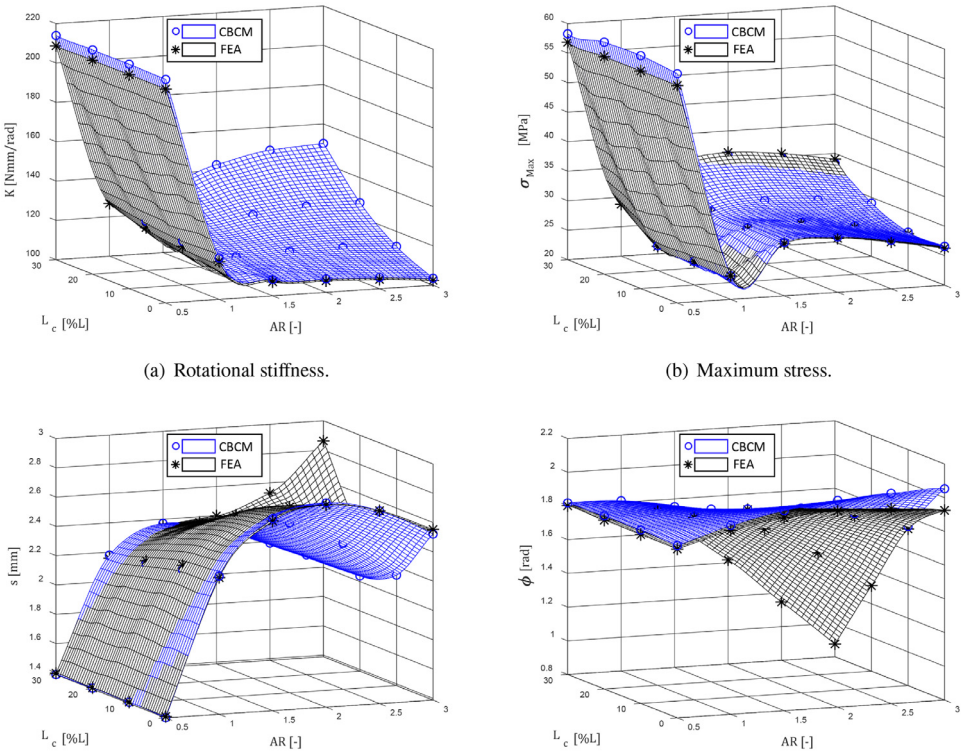

(a) Rotational stiffness.

(b) Maximum stress.

(c) Parasitic shift module.

(d) Parasitic shift phase.

Fig. 6. DOE results for $\beta = \pi/4$ rad in a pure rotation $\theta = 0.7$ rad.

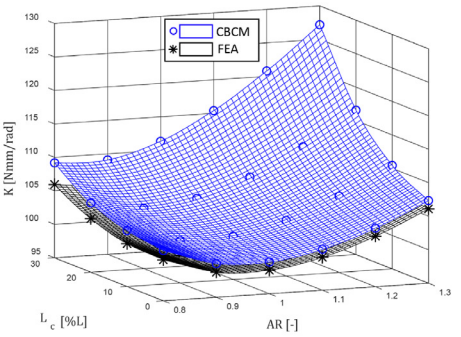

(a) Rotational stiffness.

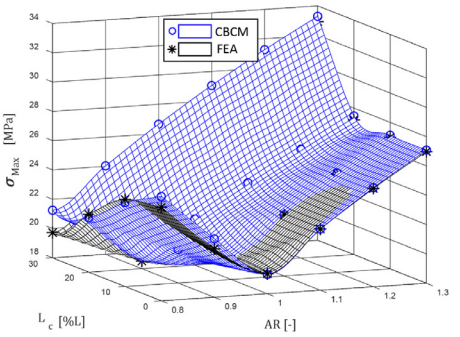

(b) Maximum stress.

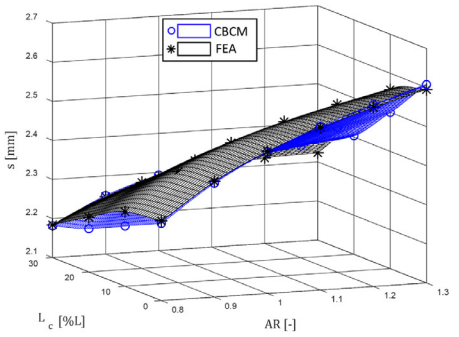

(c) Parasitic shift module.

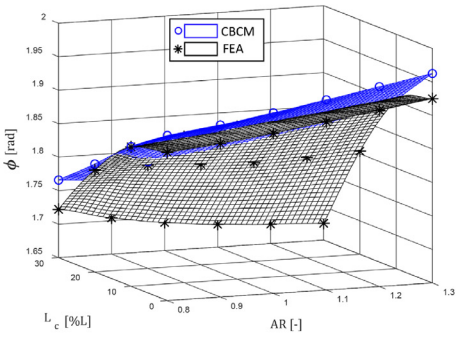

(d) Parasitic shift phase.

Fig. 7. DOE results for $L = 50$ mm in a pure rotation $\theta = 0.7$ rad.

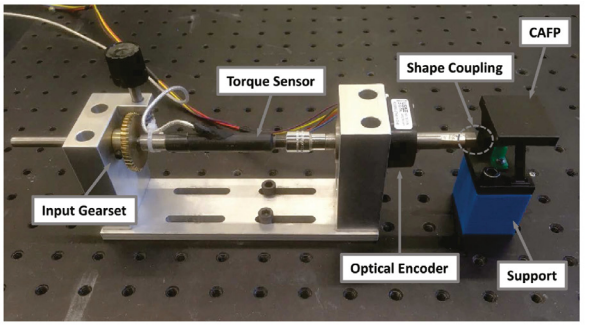

(a) Setup overview.

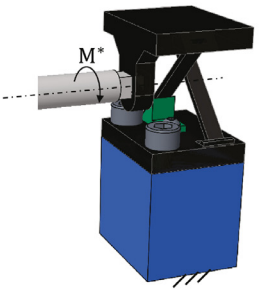

(b) Detailed view of the connection.

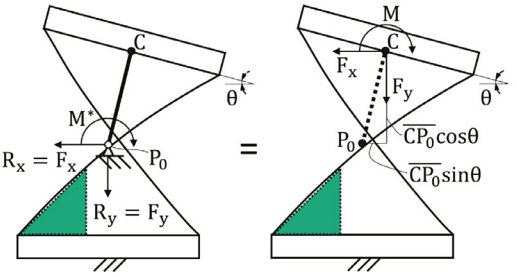

(c) Experimental load scenario.

Fig. 8. Experimental setup for stiffness evaluation.

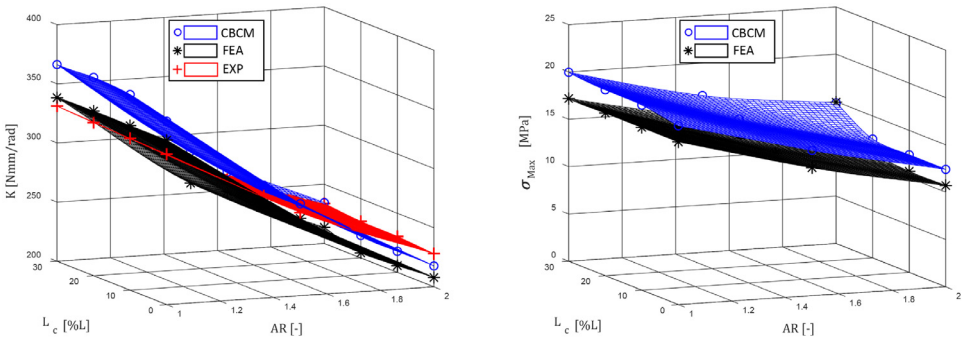

(a) Numerical and experimental stiffness. (b) Numerical maximum stress.

Fig. 9. Experimental and numerical results in pure rotation $\theta = 0.52$ rad.

Digital optical encoder with 5000 counts per revolution. A Labview interface is used to acquire the data from the sensors. The shaft is supported by bearings and is connected to the CAFP via a shape coupling, as shown in Fig. 8(b). Each candidate, characterized by a specific combination of AR and L_c, is fixed to the ground through a connection member (shown in blue) and it is deflected by the shaft. The experimental load scenario is depicted in Fig. 8(c): a moment M^* is applied by the shaft to the constrained point P_0, i.e. the initial intersection point between the CAFP beams. A rigid connection member between P_0 and C enforces a circular deflection path. As a direct consequence of the applied boundary conditions, the CAFP is not allowed to manifest the characteristic parasitic shift. The same results would be obtained by applying a set of forces F_x and F_y and moment M at point C, as shown in Fig. 8(c). For a deflection θ, the following relations hold:

$$R_x = F_x \quad R_y = F_y \quad M^* = M - F_x\overline{CP_0}\cos\theta + F_y\overline{CP_0}\sin\theta \tag{25}$$

To comply with the new load scenario, both CBCM and FEA models have been modified. In particular, a rigid segment connecting the output link to P_0 is used in the FE model, whereas a new global moment equilibrium, previously described by Eq. (10), has been defined in the CBCM with respect to P_0:

$$\begin{aligned} M^* = {} & \frac{EI}{L_{el}} m_N + \frac{EI}{L_{el}} m_{2N} + \frac{EI}{L_{el}^2}\begin{bmatrix} -(Y_A - (w_1/2\tan\beta)) & X_A \end{bmatrix}\begin{bmatrix} -\sin\beta & -\cos\beta \\ \cos\beta & -\sin\beta \end{bmatrix}\begin{bmatrix} p_{N+1} \\ f_{N+1} \end{bmatrix} \\ & + \frac{EI}{L_{el}^2}\begin{bmatrix} -(Y_B - (w_1/2\tan\beta)) & X_B \end{bmatrix}\begin{bmatrix} \sin\beta & -\cos\beta \\ \cos\beta & \sin\beta \end{bmatrix}\begin{bmatrix} p_1 \\ f_1 \end{bmatrix} \end{aligned} \tag{26}$$

where, by reference to Fig. 4(a), X_A, Y_A, X_B and Y_B are the coordinate of points A and B with respect to OXY:

$$\begin{bmatrix} X_A \\ Y_A \end{bmatrix} = \begin{bmatrix} -\sin\beta & -\cos\beta \\ \cos\beta & -\sin\beta \end{bmatrix}\begin{bmatrix} x_A \\ y_A \end{bmatrix} + \begin{bmatrix} w_1/2 \\ 0 \end{bmatrix} \qquad \begin{bmatrix} X_B \\ Y_B \end{bmatrix} = \begin{bmatrix} \sin\beta & -\cos\beta \\ \cos\beta & \sin\beta \end{bmatrix}\begin{bmatrix} x_B \\ y_B \end{bmatrix} - \begin{bmatrix} w_1/2 \\ 0 \end{bmatrix} \tag{27}$$

The total deflection, $\theta = 30^\circ = 0.52$ rad, is manually imposed to the CAFP in a series of static increments. The geometric dimensions refer to the values reported in Table 1. Figure 9 shows the results of the study for $AR = [1, 2]$ and $L_c = [0, 30]\%L$. The experimental stiffness, evaluated for each candidate as the mean value of $K = \partial M^*(\theta)/\partial\theta$, shows a good agreement with the numerical models. In line with the study presented in [46], the point at which the flexures cross in the undeformed state, defined by AR, strongly affects the joint stiffness. The influence of L_c is limited due to the applied boundary conditions, that guide the CAFP in an unnatural deflection, in which the contact is partially involved. Also the maximum stress, plotted in Fig. 9(b), shows a good overlap between CBCM and FEA.

6.2. Vertical setup

A vertical setup [47] is used to validate the framework in case of a single force load. By considering the same AR and L_c combinations of Section 6.1, the parasitic shift is evaluated in the deflected state. As shown in Fig. 10(a) and (b), the CAFP, fixed to the ground via a pair of screws, is vertically loaded by means of a cable and a calibrated mass $m = 0.4$ kg, resulting in a planar force equal to $F_x = 3.92$ N. The geometry of the output link has been designed to apply the force at point C (see also Fig. 4(a)). A rigid member that connects the output link to the initial center of rotation has been used as a simple way to trace the parasitic shift during the deflection of the pivot. Two separate images, acquired by a Canon EOS Rebel T6s equipped with EF-S 18-135 mm IS STM Lens Kit, are scaled and overlapped in CAD environment (PTC Creo), allowing the evaluation of the shift module s and phase ϕ. The results of the experimental activity are reported in Fig. 11 for each combination of AR and L_c. In particular, Fig. 11(a) and (b) show a comparison between numerical and experimental data, whereas Fig. 11(c) reports the maximum numerical stress acting on the pivot. Note that, as predicted by the numerical calculations providing $\sigma_{Max} < \sigma_s$, the structural integrity of each specimen has been preserved during physical testing. In

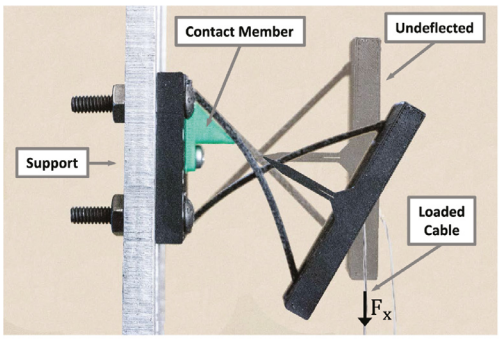

(a) Setup overview: deflected and undeflected configurations.

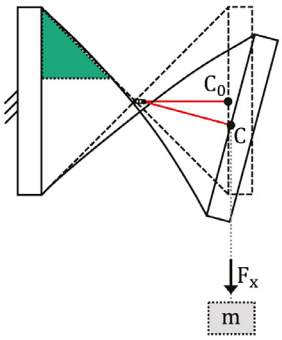

(b) Experimental load scenario.

Fig. 10. Vertical experimental setup for parasitic shift evaluation.

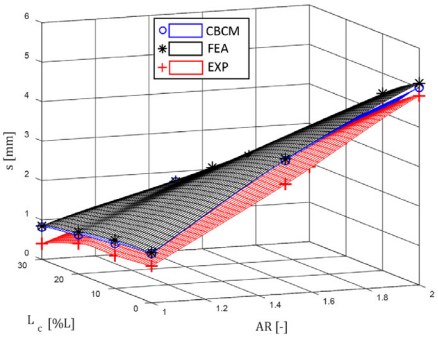

(a) Numerical and experimental parasitic shift module.

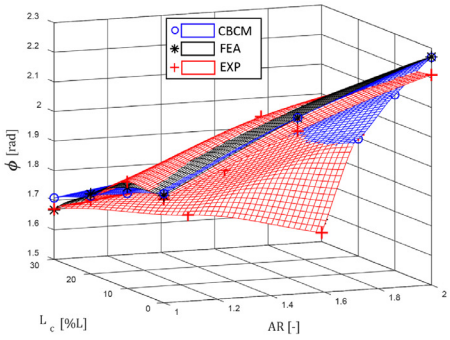

(b) Numerical and experimental parasitic shift phase.

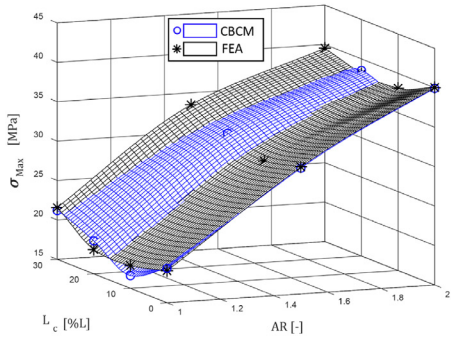

(c) Numerical maximum stress.

Fig. 11. Experimental and numerical results with a pure force $F_x = 3.92$ N.

line with the previous scenarios, the experimental assessment confirms the validity of the proposed numerical framework and underlines the accuracy of the CBCM for the modeling of contacts in large deflection problems.

7. Conclusions

This paper reports the modeling of a contact-aided CAFP, namely a system comprising a standard CAFP and a purposely shaped contact member, connected to the ground link, that acts on a single flexure. During the anti-clockwise deflection, the interaction between bodies limits the free length of the flexure, allowing a remarkable increment of the overall stiffness. The parasitic shift is also affected by the presence of the contact, as well as the stress acting on the pivot, which is an important aspect to be considered for design purposes. As examples of possible applications, the proposed device can be employed for mimicking the natural stiffness asymmetry of the human wrist, or for designing variable stiffness springs and actuation systems formed therewith. The behaviour of the pivot is numerically investigated via the CBCM technique. A multi-software

framework, comprising Matlab and ANSYS APDL, has been developed for validating the CBCM efficacy and efficiency with different planar load case scenarios. Performance maps for the pivot under a pure rotation are provided, showing a good agreement between CBCM and batch 1D FEA results for different combinations of aspect ratios and contact extensions. The limited computational time required to solve a single simulation (less than 2 s) confirms the suitability of the CBCM for parametric optimization studies. At last, 3D printed specimens of the contact-aided CAFP have been tested experimentally by means of two special purpose test rigs. All the acquired data showed good agreement with the behaviour predicted by CBCM and FEA.

Acknowledgments

The authors gratefully acknowledge Amanda Lytle for supporting in the manufacturing process and Mario Baggetta for the assistance in the image processing.

Supplementary material

Supplementary material associated with this article can be found, in the online version, at doi:10.1016/j.mechmachtheory.2019.103618.

References

[1] L.L. Howell, Compliant Mechanisms, John Wiley & Sons, 2001.
[2] J.A. Haringx, The cross-spring pivot as a constructional element, Flow Turbul. Combust. 1 (1) (1949) 313.
[3] P.P. Valentini, E. Pennestrì, Elasto-kinematic comparison of flexure hinges undergoing large displacement, Mech. Mach. Theory 110 (2017) 50–60.
[4] N. Lobontiu, Compliant Mechanisms: Design of Flexure Hinges, CRC Press, 2002.
[5] G. Berselli, A. Guerra, G. Vassura, A.O. Andrisano, An engineering method for comparing selectively compliant joints in robotic structures, IEEE/ASME Trans. Mechatron. 19 (6) (2014) 1882–1895.
[6] W.H. Wittrick, The theory of symmetrical crossed flexure pivots, Aust. J. Chem. 1 (2) (1948) 121–134.
[7] S. Bi, S. Zhang, H. Zhao, Quasi-constant rotational stiffness characteristic for cross-spring pivots in high precision measurement of unbalance moment, Precis. Eng. 43 (2016) 328–334.
[8] Y.-j. Choi, S.V. Sreenivasan, B.J. Choi, Kinematic design of large displacement precision XY positioning stage by using cross strip flexure joints and over-constrained mechanism, Mech. Mach. Theory 43 (6) (2008) 724–737.
[9] Z. Hongzhe, B. Shusheng, Y. Jingjun, G. Jun, Design of a family of ultra-precision linear motion mechanisms, J. Mech. Robot. 4 (4) (2012).
[10] L. Liu, S. Bi, Q. Yang, Y. Wang, Design and experiment of generalized triple-cross-spring flexure pivots applied to the ultra-precision instruments, Rev. Sci. Instrum. 85 (10) (2014) 105102.
[11] J. Dearden, C. Grames, J. Orr, B.D. Jensen, S.P. Magleby, L.L. Howell, Cylindrical cross-axis flexural pivots, Precis. Eng. 51 (2018) 604–613.
[12] W.J. Rundle, Design and performance of an optical mount using cross-flexure pivots, SPIE Proc. 1167 (1989) 306–312.
[13] J. Martin, M. Robert, Novel flexible pivot with large angular range and small center shift to be integrated into a bio-inspired robotic hand, J. Intell. Mater. Syst. Struct. 22 (13) (2011) 1431–1437.
[14] E.G. Merriam, J.E. Jones, S.P. Magleby, L.L. Howell, Monolithic 2 DOF fully compliant space pointing mechanism, Mech. Sci. 4 (2) (2013) 381–390.
[15] E.G. Merriam, J.M. Lund, L.L. Howell, Compound joints: behavior and benefits of flexure arrays, Precis. Eng. 45 (2016) 79–89.
[16] E.G. Merriam, L.L. Howell, Non-dimensional approach for static balancing of rotational flexures, Mech. Mach. Theory 84 (2015) 90–98.
[17] F.M. Morsch, J.L. Herder, Design of a generic zero stiffness compliant joint, in: Proceedings of the ASME International Design Engineering Technical Conferences and Computers and Information in Engineering Conference, 2010, pp. 427–435.
[18] E.G. Merriam, K.A. Tolman, L.L. Howell, Integration of advanced stiffness-reduction techniques demonstrated in a 3D-printable joint, Mech. Mach. Theory 105 (2016) 260–271.
[19] H. Zhao, C. Zhao, S. Ren, S. Bi, Analysis and evaluation of a near-zero stiffness rotational flexural pivot, Mech. Mach. Theory 135 (2019) 115–129.
[20] E.G. Merriam, L.L. Howell, Lattice flexures: geometries for stiffness reduction of blade flexures, Precis. Eng. 45 (2016) 160–167.
[21] T.G. Nelson, A. Avila, L.L. Howell, J.L. Herder, D.F. Machekposhti, Origami-inspired sacrificial joints for folding compliant mechanisms, Mech. Mach. Theory 140 (2019) 194–210.
[22] S. Bi, Y. Li, H. Zhao, Fatigue analysis and experiment of leaf-spring pivots for high precision flexural static balancing instruments, Precis. Eng. 55 (2019) 408–416.
[23] H. Zhao, S. Bi, Stiffness and stress characteristics of the generalized cross-spring pivot, Mech. Mach. Theory 45 (3) (2010) 378–391.
[24] S. Zelenika, F. De Bona, Analytical and experimental characterisation of high-precision flexural pivots subjected to lateral loads, Precis. Eng. 26 (4) (2002) 381–388.
[25] Z. Hongzhe, B. Shusheng, Accuracy characteristics of the generalized cross-spring pivot, Mech. Mach. Theory 45 (10) (2010) 1434–1448.
[26] H. Zhao, S. Bi, J. Yu, A novel compliant linear-motion mechanism based on parasitic motion compensation, Mech. Mach. Theory 50 (2012) 15–28.
[27] K. Marković, S. Zelenika, Optimized cross-spring pivot configurations with minimized parasitic shifts and stiffness variations investigated via nonlinear FEA, Mech. Based Des. Struct. Mach. 45 (3) (2017) 380–394.
[28] S. Bi, Y. Yao, S. Zhao, J. Yu, Modeling of cross-spring pivots subjected to generalized planar loads, Chin. J. Mech. Eng. 25 (6) (2012) 1075–1085.
[29] B.D. Jensen, L.L. Howell, The modeling of cross-axis flexural pivots, Mech. Mach. Theory 37 (5) (2002) 461–476.
[30] P.P. Valentini, E. Pezzuti, Design and interactive simulation of cross-axis compliant pivot using dynamic splines, Int. J. Interact. Des. Manuf. (IJIDeM) 7 (4) (2013) 261–269.
[31] S. Awtar, A.H. Slocum, E. Sevincer, Characteristics of beam-based flexure modules, J. Mech. Des. 129 (6) (2007) 625–639.
[32] S. Awtar, K. Shimotsu, S. Shiladitya, Elastic averaging in flexure mechanisms: a three-beam parallelogram flexure case study, J. Mech. Robot. 2 (4) (2010) 041006.
[33] F. Ma, G. Chen, Modeling large planar deflections of flexible beams in compliant mechanisms using chained beam-constraint-model, J. Mech. Robot. 8 (2) (2016) 021018.
[34] G. Chen, R. Bai, Modeling large spatial deflections of slender bisymmetric beams in compliant mechanisms using chained spatial-beam constraint model, J. Mech. Robot. 8 (4) (2016) 041011.
[35] G. Chen, F. Ma, G. Hao, W. Zhu, Modeling large deflections of initially curved beams in compliant mechanisms using chained beam constraint model, J. Mech. Robot. 11 (1) (2019) 011002.
[36] N.D. Mankame, G.K. Ananthasuresh, Contact aided compliant mechanisms: concept and preliminaries, in: Proceedings of the ASME International Design Engineering Technical Conferences and Computers and Information in Engineering Conference, 2002, pp. 109–121.

[37] N.D. Mankame, G.K. Ananthasuresh, Topology optimization for synthesis of contact-aided compliant mechanisms using regularized contact modeling, Comput. Struct. 82 (15–16) (2004) 1267–1290.
[38] Z. Song, S. Lan, J.S. Dai, A new mechanical design method of compliant actuators with non-linear stiffness with predefined deflection-torque profiles, Mech. Mach. Theory 133 (2019) 164–178.
[39] Y.-F. Lee, C.-Y. Chu, J.-Y. Xu, C.-C. Lan, A humanoid robotic wrist with two-dimensional series elastic actuation for accurate force/torque interaction, IEEE/ASME Trans. Mechatron. 21 (3) (2016) 1315–1325.
[40] S. Durand, C.P.-Y. Rohan, T. Hamilton, W. Skalli, H.I. Krebs, Passive wrist stiffness: the influence of handedness, IEEE Trans. Biomed. Eng. 66 (3) (2018) 656–665.
[41] P. Bilancia, G. Berselli, L. Bruzzone, P. Fanghella, A CAD/CAE integration framework for analyzing and designing spatial compliant mechanisms via pseudo-rigid-body methods, Robot. Comput. Integr. Manuf. 56 (2019) 287–302.
[42] H.-T. Pham, D.-A. Wang, A constant-force bistable mechanism for force regulation and overload protection, Mech. Mach. Theory 46 (7) (2011) 899–909.
[43] J. Choi, S. Rhim, J.H. Choi, A general purpose contact algorithm using a compliance contact force model for rigid and flexible bodies of complex geometry, Int. J. Non-Linear Mech. 53 (2013) 13–23.
[44] M. Cavazzuti, Optimization Methods: From Theory to Design Scientific and Technological Aspects in Mechanics, Springer Science & Business Media, 2012.
[45] ANSYS, ANSYS Mechanical User's Guide, ANSYS, Inc, Canonsburg, Pennsylvania, 2016.
[46] W.H. Wittrick, The properties of crossed flexure pivots, and the influence of the point at which the strips cross, Aeronaut. Q. 2 (4) (1951) 272–292.
[47] M. Yang, Z. Du, W. Dong, L. Sun, Design and modeling of a variable thickness flexure pivot, J. Mech. Robot. 11 (1) (2019) 014502.